JOURNAL OF PROPULSION AND POWER
Vol. 18, No. 2, March–April 2002

Particle Image Velocimetry Characterization of a Chordwise Bending Cascade Flowfield

Daniel A. Ehrlich* and Sanford Fleeter†
Purdue University, West Lafayette, Indiana 47907

Experiments are performed to investigate and quantify the velocity field over a chordwise-bending oscillating airfoil in a cascade operating at both design and off-design conditions. Particle image velocimetry is used to obtain a time history of the velocity field over the oscillating airfoil through one complete cycle. These data are then compared with unsteady surface-pressure data to identify the flow phenomena responsible for the cascade unsteady aerodynamic loading distributions. High leading-edge unsteady loading at zero mean incidence is attributed primarily to stagnation-point migration from upper to lower surfaces during the oscillation cycle. The unsteadiness is enhanced by the formation of a small leading-edge separation bubble that alternately grows and collapses on the upper and lower airfoil surfaces. The reduction in leading-edge unsteady loading as mean incidence is increased results in a greatly reduced stagnation-point motion that now remains on the pressure surface throughout the cycle. A substantial reduction in suction surface leading-edge velocity unsteadiness is also observed. Migration of the high-velocity region above the dynamic stall separation bubble results in increased unsteady loading between 10 and 40% chord.

Nomenclature

A_c = chordwise-bending mode shape amplitude
C = airfoil chord
C_p = unsteady surface pressure coefficient
k = reduced frequency, $\omega C/U$
p = complex airfoil surface static pressure
U = freestream velocity
V = velocity magnitude
α = cascade mean incidence angle
β = cascade interblade phase angle
θ = phase position of the oscillating airfoil
ρ = freestream density
ω = airfoil oscillation frequency

Subscripts and Superscripts

p = airfoil pressure surface
s = airfoil suction surface
1 = first harmonic of airfoil motion frequency

Introduction

RECENT efforts to increase performance and reduce size and weight of gas turbines have lead to changes in blade row design trends. Advanced turbomachinery features closely spaced blade rows that utilize thin, low-aspect-ratio blading operating under high steady loading. Also, mechanical damping is considerably reduced, particularly with integral blade–disk configurations (blisks). As a result, these configurations are subject to higher stresses at both design and off-design conditions and exhibit significant flow-induced vibration problems. With the mechanical damping considerably reduced, the motion-induced unsteady aerodynamics or aerodynamic damping of the blade row determines the vibratory response. Thus, it is important to investigate and quantify the aerodynamic damping of low-aspect-ratio blade rows, particularly the effects of off-design conditions.

The vibration characteristics of low-aspect-ratio blades more closely resemble plates than beams. They have chordwise-bending frequencies within the operating range, resulting in flow-induced chordwise-bending vibrations. Vibration modes and frequencies can be predicted with finite element analyses. However, the emphasis of unsteady aerodynamics has been on the aerodynamic damping of vibration modes of importance to high-aspect-ratio blading, for example, bending and torsion. To this end, a number of fundamental bending and torsion oscillating airfoil cascade experiments have been performed. Unfortunately, there is a dearth of fundamental unsteady aerodynamic data for the chordwise bending or two-stripe vibration modes of low-aspect-ratio blades.

The chordwise bending unsteady aerodynamics of a flat-plate cascade in subsonic flow have been investigated.[1,2] Cascade unsteady loading data were obtained utilizing an influence-coefficient technique over a range of mean flow incidence angles and reduced frequencies, simulating both design and off-design conditions. The loading data indicated significant effects of mean incidence on the cascade unsteady aerodynamics, which deviate significantly from linearized analysis predictions, with these deviations attributed to both steady loading and leading-edge separation effects.

To gain further insight into mean flow incidence and leading-edge separation effects on chordwise-bending unsteady aerodynamics, the unsteady flowfield over a chordwise-bending cascade airfoil is investigated using particle image velocimetry (PIV), a relatively new, whole-field, laser-based velocity measurement technique. The midspan-plane flowfield over the oscillating airfoil is quantified at a series of discrete instants during a single cycle of chordwise-bending airfoil oscillation. These data are then correlated with previously obtained data.[1,2] The time-resolved full-field velocity data obtained in conjunction with the unsteady loading provide a complete characterization of the chordwise-bending cascade unsteady aerodynamics including the effects of leading-edge separation.

Experimental Facility

The experiments are conducted in the Purdue Annular Cascade Research Facility (Fig. 1). It is an open-loop draw-through annular wind tunnel with a 125-cm (50-in.) o.d. and a 96-cm (38-in.) i.d. A centrifugal fan downstream of the test section driven by a 224-kW (300-hp) induction motor draws air through the facility. This fan is capable of producing steady test section velocities ranging from 6.4

Received 6 October 2000; revision received 23 June 2001; accepted for publication 2 July 2001. Copyright © 2001 by Daniel A. Ehrlich and Sanford Fleeter. Published by the American Institute of Aeronautics and Astronautics, Inc., with permission. Copies of this paper may be made for personal or internal use, on condition that the copier pay the $10.00 per-copy fee to the Copyright Clearance Center, Inc., 222 Rosewood Drive, Danvers, MA 01923; include the code 0748-4658/02 $10.00 in correspondence with the CCC.

*Research Assistant, School of Mechanical Engineering, 1288 Mechanical Engineering.
†McAllister Distinguished Professor, School of Mechanical Engineering, 1288 Mechanical Engineering. AIAA Fellow.

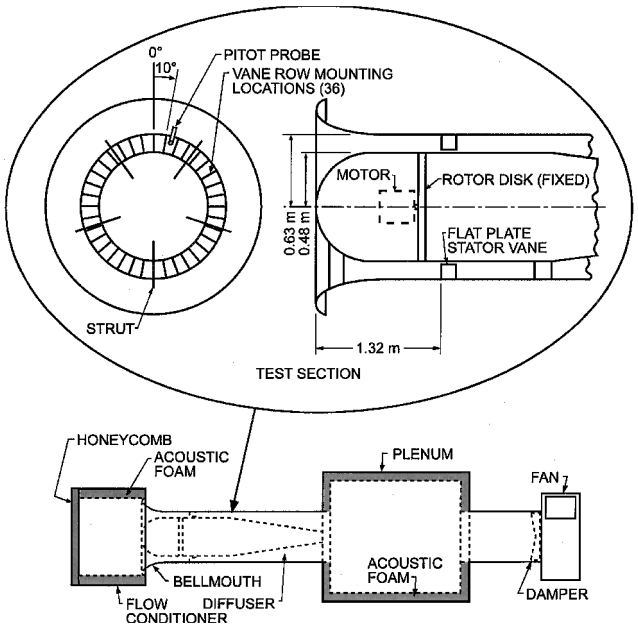

Fig. 1 Purdue annular cascade research facility.

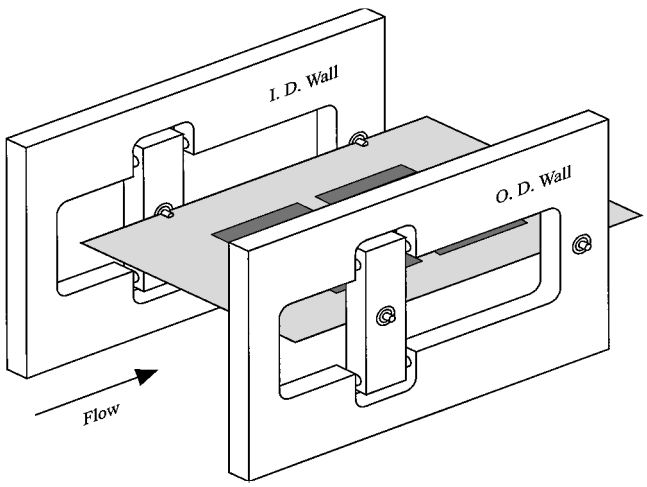

Fig. 2 Chordwise-bending oscillating airfoil.

to 70 m/s (20 to 220 ft/s). The test section is configured with an isolated row of 36 flat plate airfoils with a 17.8-cm (7.0-in.) chord and a 15-cm (5.9-in.) span, that is, a 0.85 aspect ratio, and a solidity of 1.83. Of the 36 airfoils, 35 are rigid flat plates with a thickness of 0.48 cm (0.1875 in.). The final airfoil is the chordwise-bending oscillating airfoil.[1,2]

Chordwise-bending cascade flutter conditions are simulated by a single oscillating flat plate airfoil designed to resonate in a two-dimensional, chordwise-bending mode when harmonically excited at a frequency of 66 Hz. The airfoil is constructed from a thin stainless-steel plate with shafts affixed to the hub and tip at 20 and 80% chord. These shafts are mounted in radial bearings in the cascade o.d. and i.d. endwalls and position the airfoil in the cascade to impose plate motion boundary conditions that produce the two-dimensional, chordwise-bending mode. Chordwise-bending oscillations are induced by a set of four surface-bonded piezoceramic motor elements. The oscillating airfoil mounting configuration is shown in Fig. 2. The PIV technique utilized requires optical access to the flowfield over the oscillating airfoil. Thus, the mounting configuration has been modified from that used in the previous experiments to provide optical access to the flowfield 2.2 cm (0.87 in.) above and below the airfoil surfaces. However, because of the airfoil mounting configuration, it was not possible to obtain optical

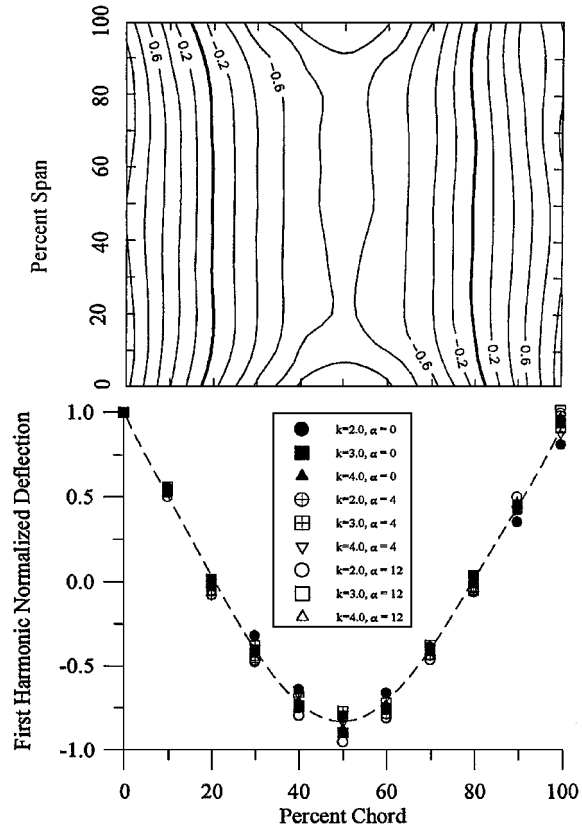

Fig. 3 Oscillating airfoil modeshape.

access in narrow regions near the 20 and 80% chord mounting shaft locations.

The chordwise-bending motion is shown in Fig. 3 by the normalized first harmonic mode shape data at reduced frequencies of 2, 3, and 4. Both a surface displacement contour plot and a midspan cross section are presented with all displacements normalized by the leading-edge midspan displacement. The nearly straight chordal contour lines indicate that the airfoil oscillates in a two-dimensional mode that exhibits two chordal node lines identified as bold contours at the shaft locations. The midspan cross section mode data exhibit a very slight dependence on reduced frequency and incidence angle.

PIV

PIV is an innovative whole-field velocity measurement technique that provides visualization and quantitative measurement of a two-dimensional velocity field. As schematically shown in Fig. 4, a PIV system comprises a high-powered laser light source, optics to generate a planar light sheet, a high-resolution digital camera, timing controls, and a computer controller and display. With PIV, whole-field velocity data are obtained by seeding the flow and measuring the distance seed particles travel over a known time interval. A double-pulsed laser light sheet illuminates a plane of seed particles, with the resulting double exposure captured during a single camera exposure. This produces a picture containing multiple images of individual particles. The distance traveled by the individual particles in the plane of the light sheet over the known time interval between laser pulses are then evaluated through correlation techniques. Constraints on the technique include a small velocity component out-of-the plane of the light sheet to minimize single particle images.

The PIV configuration used to interrogate the midspan flowfield over the chordwise-bending airfoil is shown in Fig. 5. A Spectra Physics PIV-400 Nd:YAG double-pulsed laser specially designed for PIV applications is used. It contains two independent oscillators, each capable of a maximum energy discharge of 400 mJ per pulse at a wavelength of 532 nm (green visible light) with a pulse width of approximately 6-ns duration. Two independent oscillators are

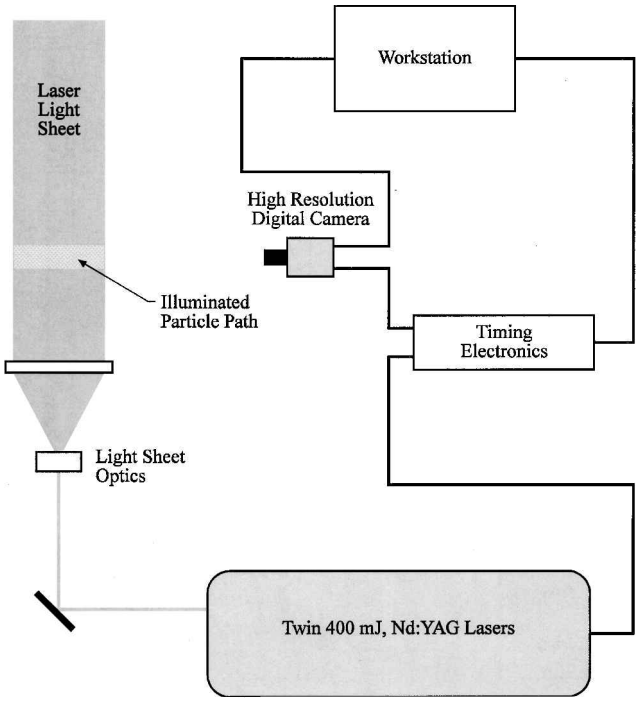

Fig. 4 Typical PIV system schematic.

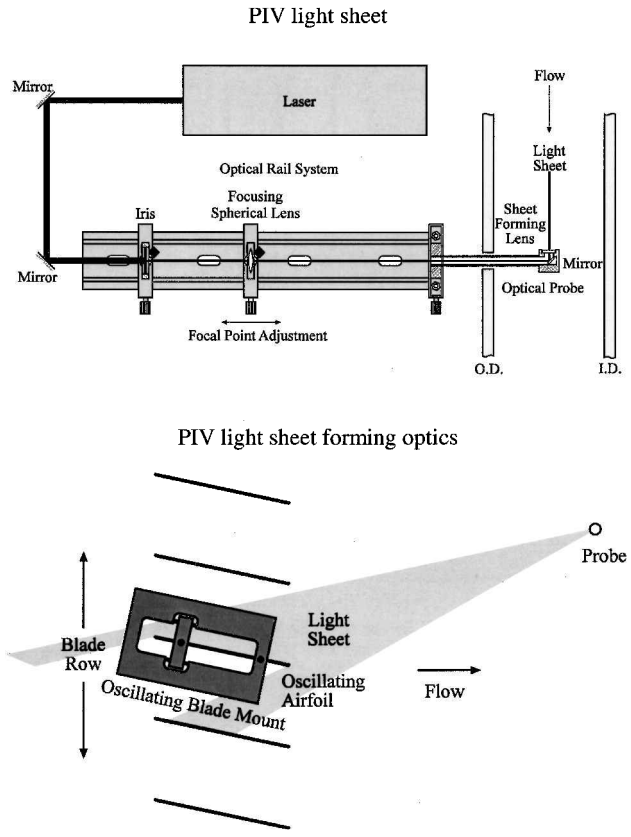

Fig. 5 PIV experimental setup.

required to provide the pair of equal energy laser pulses in the short time interval required to double expose particle images in a high-speed flow. Optics internal to the laser steer both beams to the target along the same path. Laser pulse separation is controlled through digital electronics and can be varied between 0.1 and 999.9 μs.

The midspan flowfield over the chordwise-bending oscillating airfoil is illuminated by a light sheet directed axially through the test section with its plane normal to the oscillating airfoil surface as shown in Fig. 5a. This light sheet is formed and directed to the test section by the optics train shown in Fig. 5b, which is composed of an optical rail system mounted external to the cascade and an optical probe inserted into the cascade annulus through the o.d. endwall, 50.8 cm (20 in.) downstream of the airfoil row trailing edge. The probe is inserted normal to the flow direction and parallel to the radial line on which the oscillating airfoil is positioned.

The laser pulses are directed to the light sheet forming optics train by a series of mirrors. The beam then passes through an iris mounted on the optical rail that passes only the 5-mm-(0.2-in.-) diam central portion of the beam, ensuring that the beam does not contact the inner walls of the optical probe and eliminating beam distortion introduced by the beam steering mirrors. A 1.0-m focal length cylindrical lens also mounted on the optical rail focuses the beam and ultimately positions the light sheet waist. The laser beam then enters the optical probe mounted at the end of the optical rail aligned with the beam axis. The optical probe, which is inserted into the flow, is a 20.3-cm (8-in.) long, 1.6-cm (0.625-in.) o.d., thick-wall aluminum tube fitted with a 2.54-cm-(1.0-in.-) diam probe head containing a 45-deg beam steering mirror and a 12.7-mm (0.5-in.) focal length cylindrical lens. After traveling down the probe axis, the beam strikes the mirror and is turned 90 deg and directed upstream toward the airfoil row in the axial flow direction. Finally, before exiting the probe, the beam passes through the sheet forming cylindrical lens that fans out the beam into a light sheet wide enough to illuminate the flow over an airfoil surface.

Images of particles illuminated in the flow by the laser light sheet are acquired by a Kodak 4.2 Megaplus charge-coupled device (CCD) camera with 2029×2044 active pixels through a thin, flat optical window installed in the cascade o.d. endwall. The double-exposed PIV images are displayed and analyzed on an IBM RISC 6000 Workstation using Fluid Flow Diagnostics Mark IV "On-Line" PIV software. Video images can be stored or immediately processed online to obtain scaled velocity information.

Seed particles are produced using a Rosco 1600 smoke/fog generator that produces the large volume of monodisperse aerosol required for uniform seeding of the high-volume flow. This aerosol, produced from a propylene-glycol-based fog solution, is introduced into the cascade flow through the bell mouth inlet. The seed particles range in size from 0.5 to 5.0 μm, which is much smaller than the size needed to track the velocity field.

Data Acquisition and Analysis

To characterize the unsteady flow over the oscillating airfoil through a complete cycle, instantaneous PIV midspan velocity data are obtained at a series of discrete airfoil positions. To obtain a single airfoil position velocity field in this time sequence, the PIV data acquisition is triggered at a specific point in the cycle. PIV camera, laser, and image acquisition timing are controlled by a Macintosh IIfx computer with a counter/timer board and LabView data acquisition and analysis software. The computer receives a trigger signal generated by a linear taper precision potentiometer affixed to a front oscillating airfoil mounting shaft. The output of this potentiometer is calibrated against the airfoil leading-edge midspan deflection. Thus, the signal provides the instantaneous position of the leading edge of the chordwise-bending airfoil. This timing system allows velocity data to be obtained at a specified airfoil position to within $\pm 0.6\%$ (2-deg phase) of an oscillation period.

Double-exposed images from the CCD camera are processed using the PIV image analysis software to calculate an instantaneous velocity field over the oscillating airfoil. A 2000 point grid with 1-mm^2 grid spacing is first superimposed on the 200×20 mm (8×0.8 in.) double-exposed image of the flowfield. The centroids of all of the particles in a square interrogation region around the grid point are calculated, and a digital autocorrelation performed. The autocorrelation determines the distances between all possible combinations of these particles. The most frequently occurring travel distance measured in the interrogation region is used to determine

the velocity at the grid point. The velocity computed at each grid point represents a spatial average over the interrogation region.

To achieve a signal-to-noise ratio yielding a relatively complete velocity field over the airfoil surface from the PIV images acquired, it was necessary to specify a 60 square pixel interrogation region for image analysis. Thus, each computed velocity in the field represents a spatial average of the flowfield velocity over the 8-mm^2 (0.32-in.^{2}) area around the grid point. This resolution limit is imposed by the requirement that flow over one surface of the airfoil be imaged onto a finite resolution CCD. Although the spatial resolution is inadequate to provide detailed flow information within either separated-flow regions or shed-vortex structures, the spatially averaged flow does provide information about the inviscid core flow through the cascade that is primarily responsible for imposing the blade surface-pressure distribution. The information contained within the acquired flow is, therefore, useful in interpreting the features of the unsteady loading distributions measured previously.

At each specific airfoil position, 25 PIV images are obtained. After processing each image, the resulting 25 velocity fields are averaged to provide a single ensemble-averaged field for that airfoil position. In this manner, a time history of the flowfield over the airfoil through one motion cycle is obtained. For reference, the time-average steady flowfield over the airfoil when not oscillating is also obtained from an average of 25 measured steady velocity fields. Note that 25 images were experimentally shown to yield excellent ensemble-averaged flowfields.

Experimental Procedure

The unsteady velocity field over a chordwise-bending oscillating airfoil is experimentally investigated at two cascade stagger angles. In the first case, the cascade is configured at 0-deg stagger to simulate design-point conditions, with the oscillating airfoil at a mean flow incidence angle of $\alpha = 0$ deg. Because the cascade and airfoil motion are symmetric about the oscillating airfoil mean position, velocity data are acquired for flow over only one surface of the airfoil. The velocity field over the opposite surface is then obtained by inverting the field about the airfoil mean position line and time shifting the data by one-half of an oscillation period. For example, the flowfield over the lower surface at a phase of 0 deg is obtained by inverting the flowfield measured over the upper surface at a phase of 180 deg. In the second case, the cascade airfoils are mounted at a stagger angle of 12 deg, thereby subjecting the oscillating airfoil to an $\alpha = 12$ deg mean incidence flow simulating an off-design operating condition. Velocity field data are obtained for flow over both the pressure and suction surfaces of the airfoil.

These two configurations are chosen to examine the effects of steady loading and mean flow incidence on the cascade unsteady flowfield. All data are obtained with the cascade operating at a reduced frequency of $k = 3$ with the chordwise-bending airfoil oscillating harmonically at 66 Hz with a leading-edge deflection amplitude A_c of $\pm 1.0\%$ chord corresponding to a -3–$+3$ deg change in instantaneous leading-edge angle of attack α through one motion cycle.

Previous Work

As stated earlier, the chordwise-bending unsteady aerodynamics of this cascade has been previously investigated. Using a chordwise distribution of nine dynamic-pressure transducers, the midspan unsteady loadings were measured over a range of reduced frequencies and mean flow incidence angles. The unsteady loading distributions obtained for the two cascade configurations under investigation in the current study are shown in Figs. 6 and 7. These data are provided for comparison with the time-resolved velocity field data obtained using PIV. The data are presented in the form of complex-valued first harmonic unsteady pressure difference coefficients defined by

$$\hat{C}_p^n(x) = \frac{p_1(x)}{\rho_0 U^2 (A_c/C)} \tag{1}$$

where $p_1(x)$ is the complex surface static pressure corresponding to the first harmonic of the airfoil oscillation frequency and A_c is the

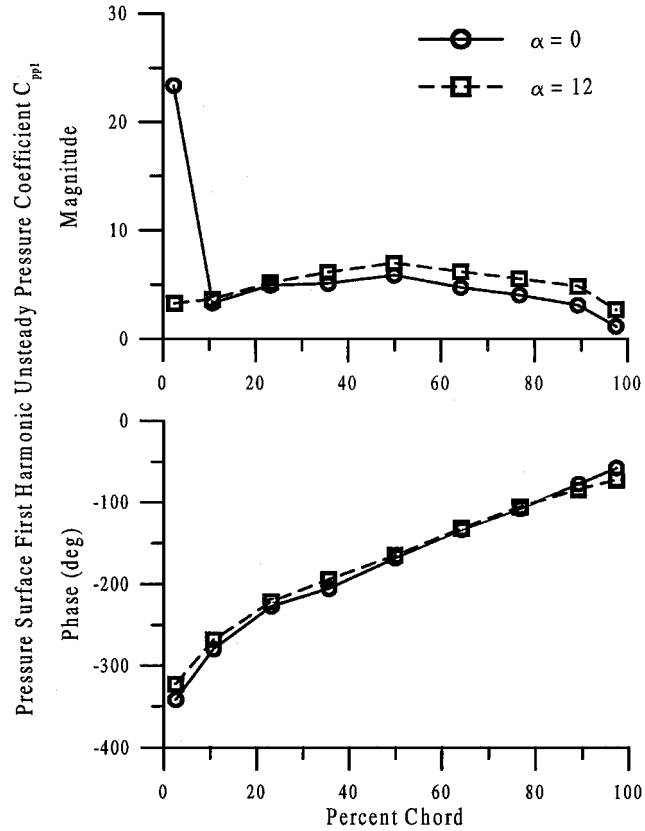

Fig. 6 Pressure surface first harmonic unsteady pressure coefficient, $k = 3$ and $\beta = 0$.

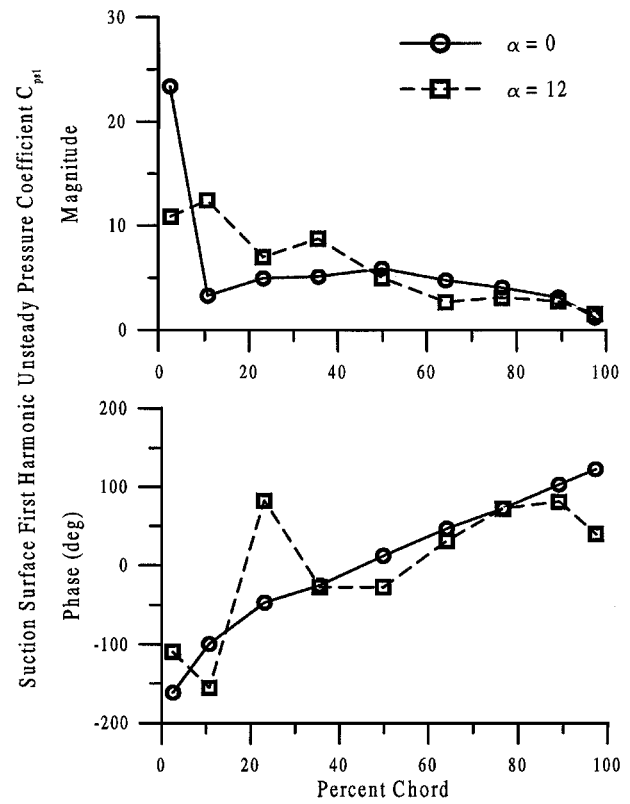

Fig. 7 Suction surface first harmonic unsteady pressure coefficient, $k = 3$ and $\beta = 0$.

chordwise-bending oscillation amplitude defined as the midspan, leading-edge airfoil deflection.

Figure 6 shows the pressure surface unsteady pressure coefficients measured for $\alpha = 0$ and 12 deg mean incidence cascades. These data indicate a dramatic decrease in leading-edge unsteady loading with increased cascade mean incidence angle, with the large leading-edge peak observed at zero mean incidence completely absent in the 12-deg cascade. However, the 12-deg cascade exhibits increased steady loading over the remainder of the pressure surface. On the suction surface (Fig. 7) increasing the mean incidence also decreases the leading-edge unsteady-pressure magnitude, but the effect is not as pronounced as on the pressure surface. Here, the leading-edge unsteady loading peak is not completely eliminated but is reduced by 54% at positive incidence. Between 10 and 50% chord, increased incidence results in a significantly increased unsteady loading. Finally, over the aft-half of the airfoil, reduced unsteady loading is seen on the 12-deg cascade as compared to the 0-deg cascade. The objective of the current experiments is to resolve the cascade velocity fields adequately to identify the flow phenomena responsible for the described unsteady loading distributions.

Experimental Results and Discussion

Time-averaged velocity fields in the form of velocity-magnitude contour plots are shown in Fig. 8 for both the 0- and 12-deg cascades with the chordwise-bending airfoil not oscillating. These are provided as reference for the unsteady flowfield sequences. The flat-plate airfoil is schematically represented by a bold line in the center of each velocity field, with flow from left to right. Solid circles at 20 and 80% chord represent the airfoil mounting shafts and bearings. Two rectangular boxes are also shown around the mounting shafts to indicate the portion of the flow obscured by the oscillating airfoil mounting system. Finally, white areas within the flowfield represent regions over which the image analysis software is unable to determine velocities with an acceptable signal-to-noise ratio.

The zero mean incidence cascade approach flow is uniform. As the flow enters the passage, acceleration due to the potential field of the cascade is evident. Recall, symmetry of the flow with respect to the airfoil centerline is assumed with upper and lower surface flowfields represented by the same data to provide a complete picture. White voids seen in the velocity field aft of the front and forward of the rear mounting shafts are due to obstruction of optical access by lead wires that power the piezoelectric drive crystals on the airfoil surface and are typical of all velocity data presented herein. The inability to obtain velocity measurements near the surface of the airfoil trailing edge is the result of light sheet surface reflections that degrade the PIV image signal-to-noise ratio.

The positive-incidence ($\alpha = 12$ deg) cascade steady flowfield presents a much more interesting picture. The most prevalent feature is the large white region over the airfoil suction surface where no velocity data are obtained. The source of this void in the data is conjectured to be fully separated flow over the suction surface. This hypothesis is supported by close examination of the raw unprocessed PIV images, where the seeded flow provides useful flow visualization information. In these images, considerable differences were apparent between this region and the remainder of the flowfield where velocity data are obtained. Furthermore, images for the pressure surface flowfield of this airfoil and the $\alpha = 0$ deg cascade flow, where relatively uniform attached flows are expected, yield complete velocity fields under identical data acquisition conditions. As already stated, the inability to obtain velocity data on the suction surface is likely a result of an inability to spatially resolve the flow structures in this separated flow region.

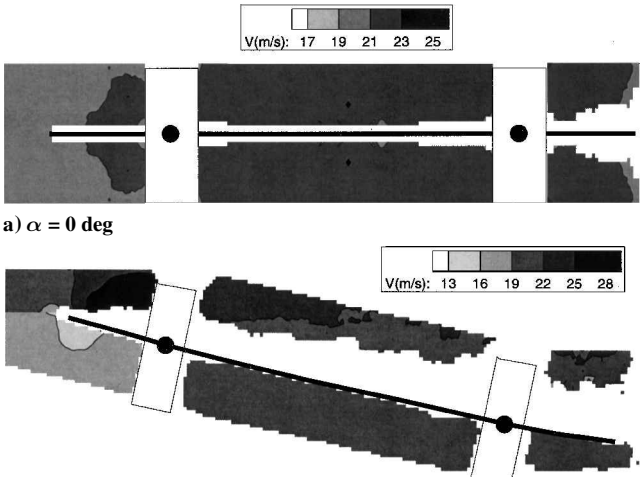

Fig. 8 Steady flow velocity magnitude contours.

The presence of this suction surface data void presented some difficulty in obtaining the average flowfield presented in Fig. 8b. The data shown are a time average of 25 instantaneous images, each having slightly different regions where velocity data are unobtainable due to the turbulent nature of the separated flow. The time-averaged location of the separated flow region (represented by the absence of velocity data) is obtained by averaging the velocity fields assuming that a grid point location lies inside a separated zone in the mean if the grid point yielded no velocity data at least 22 of 25 times. This implies that a grid point in the separated zone in the time-averaged data represents a point in the separated zone of the instantaneous data 88% of the time. This same technique is used to locate separated flow regions and shed vortex structures in the ensemble-averaged unsteady velocity data.

The flow over the suction surface of the 12-deg cascade airfoil is highly influenced by the large separated flow region. The inlet flow accelerates rapidly over the large flow blockage, reaching a maximum velocity at approximately 10% chord before decelerating behind the maximum thickness part of the blockage at 20% chord. On the pressure surface, a region of low-velocity flow near the leading edge is associated with the stagnation point. This smearing of the stagnation-point flow is due to the spatial averaging introduced by the size of the PIV interrogation region. The pressure surface flow accelerates slightly due to the blockage effects caused by the adjacent airfoil, becoming uniform as it enters the midchord region in the airfoil row. Finally, the line discontinuity between pressure and suction surface flowfields near the leading edge is attributed to the independent processing of the pressure and suction surface data causing the acceleration over the suction surface and the deceleration at the pressure surface stagnation point to bias the two spatially averaged approach flows differently.

Zero Mean Incidence (α = 0 Degrees) Unsteady Velocity Field

Velocity data obtained with the airfoil oscillating in the chordwise-bending mode are presented as a sequence of velocity magnitude contour plots at each of eight discrete airfoil positions during the motion cycle. The eight velocity fields, separated in time by one-eighth cycle (45-deg phase), represent a single cycle time history of the flowfield. Figure 9 shows the eight discrete airfoil positions for which velocity field data are obtained. The amplitude of oscillation has been greatly exaggerated for illustration purposes. The reference or $\theta = 0$ deg position in the cycle is taken with the airfoil leading edge moving upward and the airfoil in the undeflected position, as shown in Fig. 9a.

Figures 10 and 11 present a time history of the ensemble-averaged unsteady flowfield at zero mean incidence. The eight velocity fields ($\theta = 0, 45, 90, 135, 180, 225, 270$, and 315 deg) illustrate changes in the flow through one complete cycle. Several features of the unsteady flowfield are readily apparent. First, the approach flow to the cascade remains uniform and constant magnitude throughout the entire cycle and is identical to the steady approach flow shown in Fig. 8a. This suggests that the unsteady potential effects of the oscillating airfoil are limited to a small region near the airfoil surface as is expected for a small-amplitude harmonic oscillation.

Second, a low-velocity region again attributed to the effect of the stagnation-point flow on the spatially averaged data appears near the leading edge. This low-velocity region first appears on the lower surface at $\theta = 45$ deg, persisting through $\theta = 90$ deg at maximum

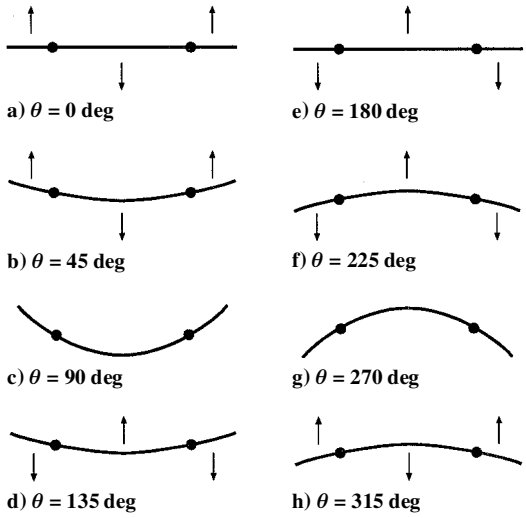

Fig. 9 Chordwise-bending oscillation cycle data acquisition airfoil positions.

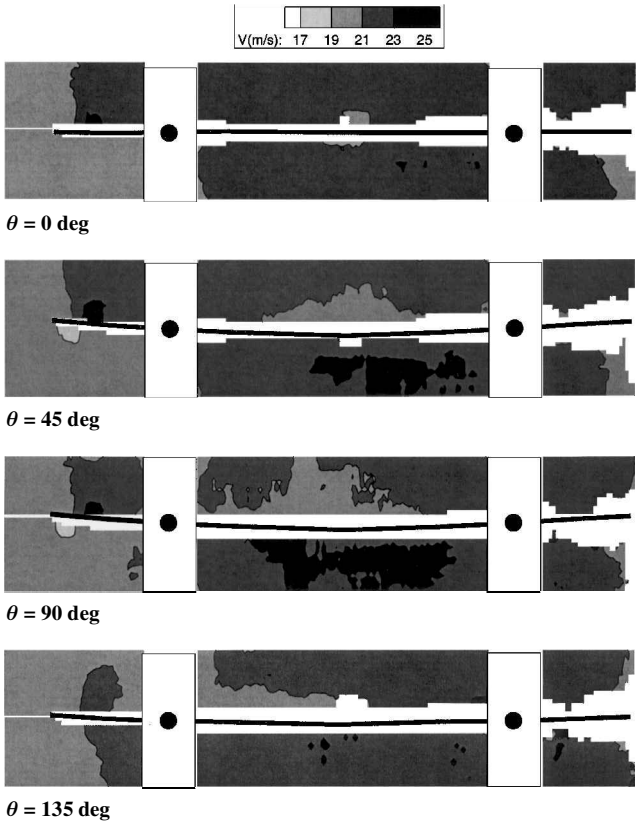

Fig. 10 Chordwise-bending velocity magnitude contour time-sequence, α = 0 deg and θ = 0–135 deg.

leading-edge upward deflection before collapsing as the leading edge reverses direction and begins to move back toward its mean position. The low-velocity region next appears on the upper surface at $\theta = 225$ and 270 deg after the airfoil moves through its mean position toward the maximum leading-edge downpoint. Thus, this low-velocity region appears only where a stagnation point is expected near the leading edge on the airfoil pressure surface when instantaneously cambered due to the chordwise-bending motion. Consequently, the data suggest that the stagnation point alternates surfaces moving around the airfoil leading edge as the airfoil oscillates, resulting in the high leading-edge unsteady loadings of Figs. 6 and 7.

A high-velocity region near 10% chord also alternately grows and collapses on the upper and lower airfoil surfaces over the cycle.

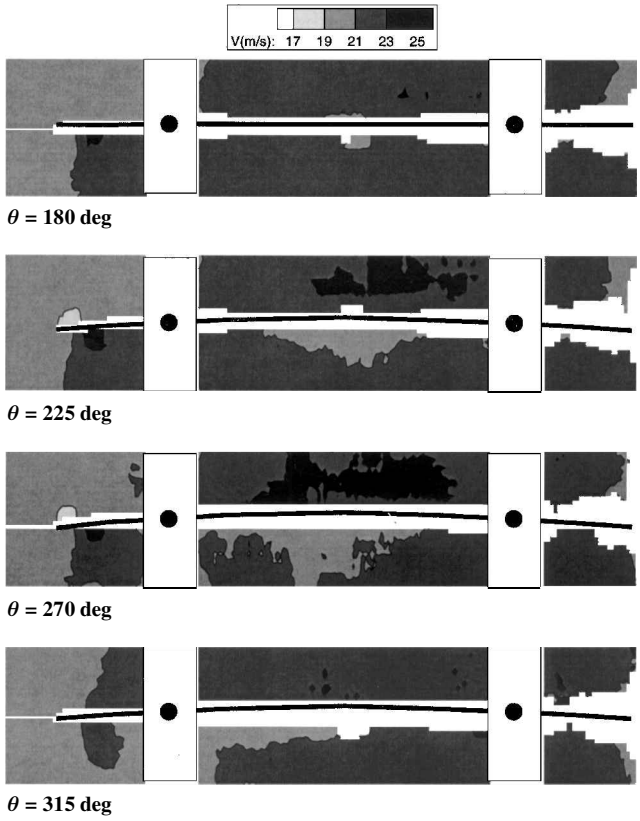

Fig. 11 Chordwise-bending velocity magnitude contour time sequence, α = 0 deg and θ = 180–315 deg.

This flowfield feature is most prevalent at $\theta = 45$ and 225 deg on the upper and lower surfaces, respectively, and is consistent with the acceleration expected around a small leading-separation bubble. Such a dynamic stall in which a separation bubble alternately forms on the upper and lower surfaces of the airfoil would also contribute to the high leading-edge unsteady loading observed in the $\alpha = 0$ deg cascade.

In the midchord region between the mounting shafts, the source of the velocity unsteadiness appears to be the unsteady potential field of the oscillating airfoil. In regions of the flow where the airfoil motion reduces the passage flow area, such as the lower surface at $\theta = 90$ deg, the flow accelerates. Conversely, where the airfoil motion increases the passage flow area, the flow decelerates. Although the resulting velocity unsteadiness appears to be on the same order as that observed in the leading-edge region, the actual leading-edge velocity gradients near the stagnation point are expected to be much larger than that which can be represented with the current interrogation region size. This would explain the relatively low midspan unsteady pressure loadings shown in Figs. 6 and 7. Finally, the trailing-edge velocity data indicate minimal velocity unsteadiness in agreement with the pressure data.

Positive Incidence (α = 12 Degree) Unsteady Velocity Field

Figures 12 and 13 present a time history of the ensemble-averaged unsteady chordwise-bending airfoil flow at 12-deg mean incidence. As for zero mean incidence, eight velocity-magnitude contour plots illustrate changes in the flowfield through one cycle.

The suction surface steady flow separation in Fig. 8b is also present throughout the oscillation cycle. However, significant dynamic effects on the size and position of the separated flow region are evident. Recall that for the 12-deg cascade steady flow, the low spatial resolution of the PIV images precluded resolving the velocity field in regions of separated flow and regions containing shed vortex structures. For this reason, the white regions of the suction surface velocity field where PIV images consistently failed to yield velocity data represent the ensemble-averaged position of a leading-edge

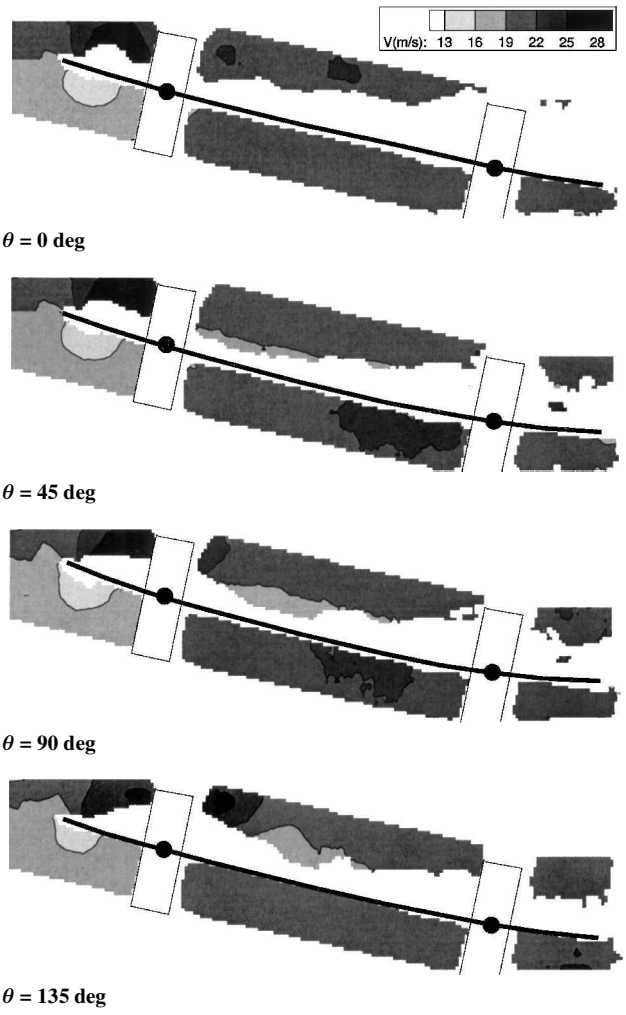

Fig. 12 Chordwise-bending velocity magnitude contour time sequence, α = 12 deg and θ = 0–135 deg.

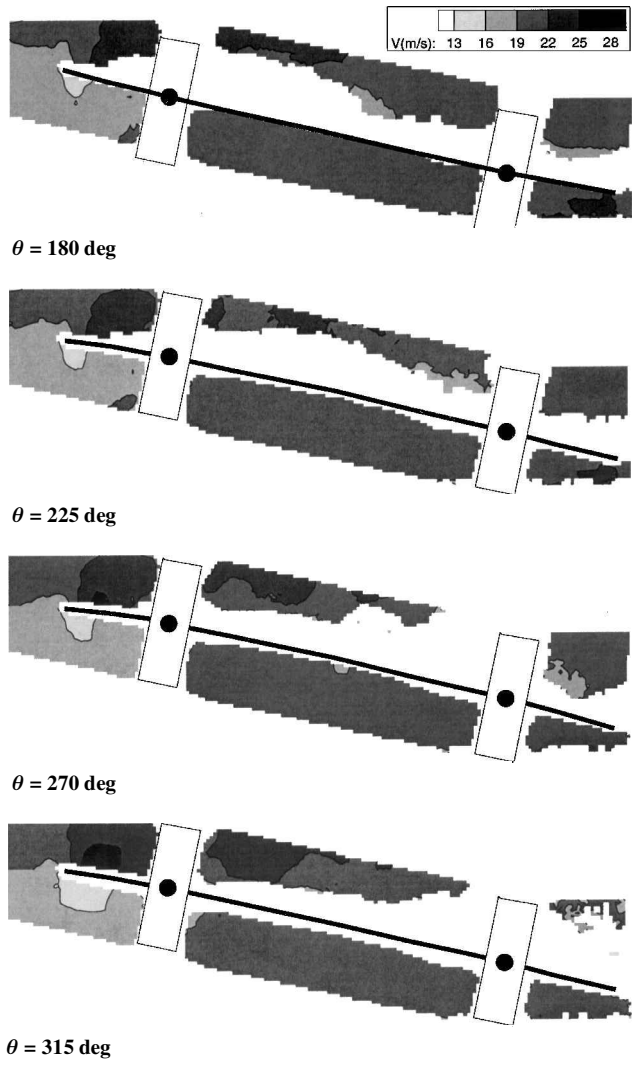

Fig. 13 Chordwise-bending velocity magnitude contour time sequence, α = 12 deg and θ = 180–315 deg.

separation bubble and downstream vortex structures shed from that bubble. Again, careful examination of the raw PIV image flow visualizations supports this hypothesis. It is also consistent with the presence of strong flow acceleration over the maximum thickness region of the leading-edge bubble at each airfoil position from $\theta = 0$ to 135 deg followed by a downstream deceleration as the flow expands into the increased flow area behind the blockage. This high-velocity region moves rearward over the airfoil surface from approximately 10% chord at $\theta = 0$ deg to 26% chord at $\theta = 135$ deg accompanied by an apparent growth in the length of the separation bubble as the leading edge of the airfoil pitches upward through maximum deflection and begins its decent toward the mean position.

At the maximum leading-edge up ($\theta = 90$ deg) airfoil position, the data capture a reattachment point behind the leading-edge separation bubble. This is best illustrated by the streamline trace plot shown in Fig. 14 obtained from instantaneous data at this airfoil position. The streamlines pass up over the separation bubble and back down to very near the airfoil surface near 39% chord.

During the second half-cycle as the airfoil leading edge pitches downward (Figs. 12 and 13), the white region near the leading edge begins to shrink, suggesting a collapse of the separation bubble. Simultaneously, the white region downstream of the leading edge grows, possibly due to the shedding of a large vortex from the downstream edge of the bubble as it collapses. This is most evident at the $\theta = 180$ and 225 deg airfoil positions where the leading edge begins to move downward, decreasing flow incidence. By the time the leading edge reaches the maximum down position at $\theta = 270$ deg, the leading-edge flow is essentially attached. Growth of a small high-speed region near the leading edge between $\theta = 270$ and 315 deg

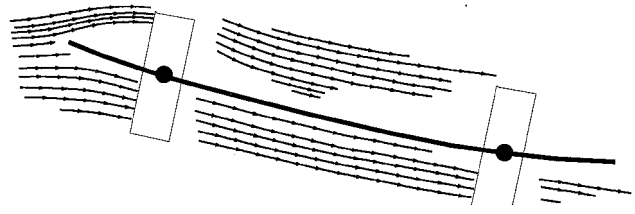

Fig. 14 Chordwise-bending flowfield streamline plot, α = 12 deg and θ = 90 deg.

may be due to the early stages of formation of the separation bubble seen at $\theta = 0$ deg.

In addition to the growth, movement, and collapse of a leading-edge separation bubble, the suction-surface near-leading-edge data exhibit another significant difference from the zero mean incidence data. The velocity field at 2.5% chord (the first transducer) is essentially steady, in contrast to the $\alpha = 0$ deg data, which showed large unsteadiness there due to the migration of the stagnation point between the upper and lower surfaces. These two phenomena suggest themselves as sources for the reduced leading-edge loading and increased loading from 10 to 40% chord on the suction surface in the $\alpha = 12$ deg cascade as compared to the $\alpha = 0$ deg cascade loading data as was shown in Fig. 7.

Flow unsteadiness on the pressure surface of the positive incidence cascade is minimal. A low-velocity region near the leading edge associated with the location of the stagnation point is

essentially stationary throughout the cycle, showing some size reduction over the part of the cycle during which the leading edge moves downward. Unlike the zero mean incidence cascade, the stagnation point on the 12-deg airfoil remains on the pressure surface at all times. With the exception of a small region of flow acceleration between 50 and 80% chord at the $\theta = 45$ and 90 deg airfoil positions, the flow over the pressure surface aft of 20% chord is essentially uniform and of constant magnitude. Thus, as on the suction surface, the decreased leading-edge unsteady loading on the pressure surface in the $\alpha = 12$ deg cascade shown in Fig. 6 is attributed to the greatly reduced movement of the stagnation point, which remains essentially stationary near the pressure surface leading edge in this cascade.

Conclusions

Experiments were performed to investigate and quantify the velocity field over a chordwise-bending oscillating airfoil in a cascade at both design and off-design incidence angles. PIV was used to obtain ensemble-averaged velocity fields at eight instantaneous airfoil positions to identify changes in the flowfield through one complete oscillation cycle. These data were then compared with previously measured unsteady surface pressure data to identify flow phenomena responsible for the cascade unsteady aerodynamic loading distributions.

High unsteady loading near the leading edge in the zero mean incidence cascade results primarily from the migration of the stagnation point from the upper to the lower surface as the airfoil moves through the cycle. A small leading-edge separation bubble that alternately grows and collapses on the upper and lower airfoil surfaces over the cycle also contributes to the high leading-edge loading. The velocity field in the midchord region shows a reduced unsteadiness associated with the unsteady potential field of the oscillating airfoil, consistent with the low unsteady loading there.

The 12-deg mean incidence cascade exhibits fully separated flow over the suction surface under steady (not oscillating) conditions. Suction surface flow separation is also present during the chordwise bending cycle, with significant dynamic effects on the size and position of the separated flow region. A leading edge separation bubble forms that increases in thickness and length as the leading edge of the airfoil pitches upward through maximum deflection and begins its decent toward the mean position. During the second half-cycle, the downstream end of the separation bubble recedes as the leading edge begins to move downward, decreasing flow incidence. The separation bubble ultimately collapses as the leading edge passes through maximum downward deflection and the leading edge flow is essentially attached. This dynamic stall behavior accounts for the increase in unsteady loading between 10 and 40% chord as the mean incidence is increased from $\alpha = 0$ to 12 deg. Also, unlike the zero mean incidence cascade, the flow velocities over the suction-surface leading-edge pressure transducer location are essentially constant, and the stagnation point is essentially stationary on the pressure surface throughout the cycle. These flow phenomena account for the reduced leading-edge unsteady loading seen in a cascade operating at high positive incidence.

Acknowledgments

This research was sponsored, in part, by the Army Research Office and the NASA John H. Glenn Research Center at Lewis Field. This support is most gratefully acknowledged.

References

[1]Ehrlich, D. A., and Fleeter, S., "Chordwise Bending Cascade Unsteady Aerodynamics by an Experimental Influence Coefficient Technique," *Journal of Propulsion and Power*, Vol. 13, No. 1, 1997, pp. 39–48.

[2]Ehrlich, D. A., and Fleeter, S., "Incidence Effects on Chordwise Bending Cascade Unsteady Aerodynamics," AIAA Paper 96-2667, 1996.